

Special
Collection

Porous Iron-Nitrogen-Carbon Electrocatalysts for Anion Exchange Membrane Fuel Cells (AEMFC)

Beatrice Ricciardi,^[a] Barbara Mecheri,^{*[a]} Williane da Silva Freitas,^[a] Valerio C. A. Ficca,^[b] Ernesto Placidi,^[b] Irene Gatto,^[c] Alessandra Carbone,^[c] Andrea Capasso,^[d] and Alessandra D'Epifanio^{*[a]}

High-performance platinum group metal-free (PGM-free) electrocatalysts were prepared from porous organic polymers (POPs) precursors with highly-porous structures and adjustable surface area. A resin phenol-melamine-based POP and an iron salt were used to synthesize Fe–N–C catalysts with different iron contents (0.2–1.3 wt.%). Electrochemical and spectroscopical characterization allowed us to elucidate the effect of Fe content on the material's structure, surface chemistry, and electrocatalytic activity toward the oxygen reduction reaction (ORR). The increase of iron content led to a specific surface area decrease, preserving the morphological structure, with the

formation of highly-active catalytic sites, as indicated by X-ray photoelectron spectroscopy (XPS) analysis. The rotating ring disk electrode experiments, performed at pH=13, confirmed the high ORR activity of both 0.5 Fe ($E_{1/2}=0.84$ V) and 1.3 Fe ($E_{1/2}=0.83$ V) catalysts, which were assembled at the cathode of a H₂-fed anion exchange membrane fuel cells (AEMFC) equipped with a FAA-3-50 membrane, evidencing promising performance (0.5 Fe, maximum power density, Max PD=69 mA cm⁻² and 1.3 Fe, Max PD=87 mA cm⁻²) with further advancement prospects.

Introduction

Over the past few years, the requirement of an energy transition to a circular economy with high efficiency and low environmental impact requires increasingly advanced strategies to meet society's demands.^[1] Hydrogen represents a strategic energy carrier to achieve a system with zero emissions impact and may be employed as a high-yield fuel.^[2] Using H₂ has found numerous applications in industry, domestic electricity, heat generation, locally stored energy, and transportation.^[3–5] The most critical obstacles to the transition to the H₂ economy arise from economic, technical, and implementation/execution issues

compared to existing and established fossil fuel-based technologies.

Hydrogen-fed anion exchange membrane fuel cells (AEMFCs) have recently gained considerable interest driven by the many advantages of AEMFC technology over the currently marketed PEMFC (proton exchange membrane fuel cell) technology.^[6] The two technologies are very similar; however, an AEMFC employs an alkaline environment compared to PEMFC. This offers several potential advantages, including using a wider choice of fuels in addition to pure hydrogen and better oxygen reduction catalysis. Pt-based or platinum group metals (PGM)-based catalysts are the benchmark catalysts for the oxygen reduction reaction of both polymeric exchange membrane fuel cells.^[7–11] Despite high activity, their high cost, environmental impact, and poor durability limit their large-scale application. PGM catalysts are responsible for more than 50% of the total cost of the fuel cell stack.^[12] They also tend to degrade and are easily poisoned by contaminants, such as CO, H₂S, and NH₃, limiting their durability.^[13–16]

Many research efforts have been devoted to developing PGM-free catalysts. Transition metal-nitrogen-carbon (M–N–C) materials have been identified as one of the most promising alternatives for the oxygen reduction reaction at the cathode side of AEMFCs.^[17–22]


Among these materials, an up-and-coming class is Fe–N–C-based catalysts, consisting of a carbon (C) matrix doped with nitrogen (N) heteroatoms and Fe.^[23–25] Fe–N_x–C moieties are primary active sites for oxygen reduction reaction (ORR) and have shown high catalytic activity, comparable to commercial Pt/C, representing the state-of-the-art.^[26–28] Often, these PGM-free catalysts' main limitation is the active sites' exposure and the optimal distribution of Fe, which must be atomically dispersed in the Fe–N_x–C moieties.^[29,30]


[a] B. Ricciardi, Prof. B. Mecheri, Dr. W. da Silva Freitas, Prof. A. D'Epifanio
Department of Chemical Science and Technologies
University of Rome Tor Vergata
Via della Ricerca Scientifica, 00133 Rome (Italy)
E-mail: barbara.mecheri@uniroma2.it
alessandra.d.epifanio@uniroma2.it


[b] Dr. V. C. A. Ficca, Prof. E. Placidi
Department of Physics
Sapienza University of Rome
Piazzale Aldo Moro 2, 00185, Rome (Italy)

[c] Dr. I. Gatto, Dr. A. Carbone
Institute for Advanced Energy Technologies "Nicola Giordano"-CNR-ITAE
Via S. Lucia Sopra Contesse 5, 98126 Messina (Italy)

[d] Dr. A. Capasso
International Iberian Nanotechnology Laboratory (INL)
Braga 4715-330 (Portugal)

 Supporting information for this article is available on the WWW under <https://doi.org/10.1002/celec.202201115>

 An invited contribution to a Special Collection dedicated to *Giornate dell'Elettrochimica Italiana 2022 (GEI2022)*

 © 2023 The Authors. ChemElectroChem published by Wiley-VCH GmbH. This is an open access article under the terms of the Creative Commons Attribution License, which permits use, distribution and reproduction in any medium, provided the original work is properly cited.

The carbon matrix plays an essential role in ORR activity, as a porous structure increases the accessibility of active sites in $M-N_x-C$.^[31] Materials with hierarchical porosity are promising as they can promote the mass transport of species involved in the ORR and high exposure of the active sites.^[32,33]

Nowadays, several ways of synthesizing $Fe-N-C$ materials are known; catalytically active materials can be obtained from the pyrolysis of a wide variety of chemical precursors containing carbon sources (conductive supports such as carbon blacks, nanotubes and graphene oxide organic molecules, and polymers), nitrogen sources (N-containing organic molecules, polymers, or reactive gas such as NH_3), and transition metal sources (e.g., a salt).^[34–36] In our approach, high-nitrogen porous organic polymers (POPs) were used as precursors for $Fe-N_x-C$ formation for ORR catalysis. Functional mesoporous materials with large surface area, large pore volume, unique mesostructures, and diverse compositions have shown potential applications in catalysis and biomedicine, as well as in adsorption and separation techniques.^[37,38]

The common strategies for preparing a porous material are based on either the hard template^[39–41] or the soft-template method.^[42,43] The hard-template approach is limited by complex synthesis steps, low product yield, and pore obstruction due to limited silica removal.^[44] By contrast, the soft-template method allows the design and synthesis of a large variety of ordered mesoporous materials thanks to the use of surfactants, which orientate precursor molecules to form a 3D structure.^[45] In comparison to the hard template method, which typically involves the use of highly concentrated acidic (HF) or alkaline solutions to remove the silica template, in the soft-template approach, a surfactant can be easily removed from the carbon structure during the pyrolysis step adopted to form the $M-N_x-C$ active sites, reducing costs and non-environmentally friendly synthesis steps, such as the silica leaching after synthesis.^[46] When using amphiphilic block copolymers as templates (such as polystyrene-block-poly(ethylene oxide)-block-polystyrene and Pluronic block copolymers), highly ordered mesoporous materials with large surface areas and uniform pore sizes (1.5–30 nm) can be obtained and used in several applications, including catalysis, gas separation, photo energy conversion in solar cells, detection and removal of pollutants/contaminants from water/others liquids and along with others essential application.^[47–49]

Here, we proposed a facile strategy for synthesizing iron-nitrogen-doped mesoporous carbon ($Fe-N-C$) catalysts, using phenol (P) as the carbon precursor, melamine (M) as the

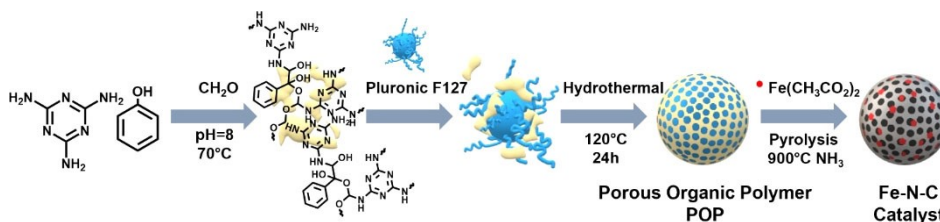
nitrogen precursor, and iron acetate.^[50] Different synthesis conditions were adopted to obtain resin phenol-melamine-based POP precursors and the role of both phenol and melamine (P/M) ratios on the materials morphology, and ORR activity performance was investigated. In addition, the effect of different metal concentrations on the porous structures was evaluated to enhance ORR activity by increasing the content of available active sites. $Fe-N-C$ electrocatalysts were obtained with high specific surface area ($512-1022\text{ m}^2\text{ g}^{-1}$), and homogeneous particles size distribution (diameter, 200–300 nm). Electrochemical characterization indicated high ORR activity, and accelerated degradation tests (ADTs) performed in a half-cell configuration showed remarkable performance for over 7500 cycles in the stress performed in N_2 -saturated electrolyte. ADTs were also performed in O_2 -saturated environment, discriminating the most promising samples (0.5 Fe and 1.3 Fe) and showing results in agreement with the tests performed in AEMFC. The POP-derived $Fe-N-C$ materials also demonstrated good activity when assembled at the cathode side of an AEMFC prototype fed with H_2 .

Results and Discussion

Different nitrogen-doped porous carbon (N-C) structures were synthesized by using phenol (P) as the carbon precursor, melamine (M) as the nitrogen precursor, and formaldehyde as a reaction electrophilic initiator.

Since material properties such as morphology and electrocatalytic performance can be tailored by modulating the molar ratio of precursors and templating agents, different phenol and melamine (P/M) ratios and Pluronic F127 (T) used as a soft templating agent were investigated and optimized.^[51,52]

The synthesis strategy is shown in Scheme 1 and produced three different samples: PMT1:2, PMT1:3, and PM1:3, depending on the P/M molar ratio and presence of T as a templating agent. The samples obtained before pyrolysis were characterized by FT-IR spectroscopy (Figure S1) confirming the presence of N-H and C-H bonds (at $\sim 3400\text{ cm}^{-1}$ and $\sim 2900\text{ cm}^{-1}$, respectively) arising from the phenol and melamine precursors. At higher wavenumbers, C=C and C=N bending can be observed, while in the fingerprint region ($1500-500\text{ cm}^{-1}$), the polymeric chain's C-O, C-N, and C-C bonds can be seen. The pyrolysis conditions are crucial to the introduction of N-based functionalities and for preventing the collapse of the hierarchical porous structure of the carbon matrix while controlling POP carbon-



Scheme 1. Synthesis of the POP-derived $Fe-N-C$ catalysts: polymerization of precursors at alkaline pH; micelle formation led by the templating agent (Pluronic F127); formation of the 3D structures after hydrothermal synthesis step and pyrolysis step to the template removal and formation of the $Fe-N_x-C$ active sites.

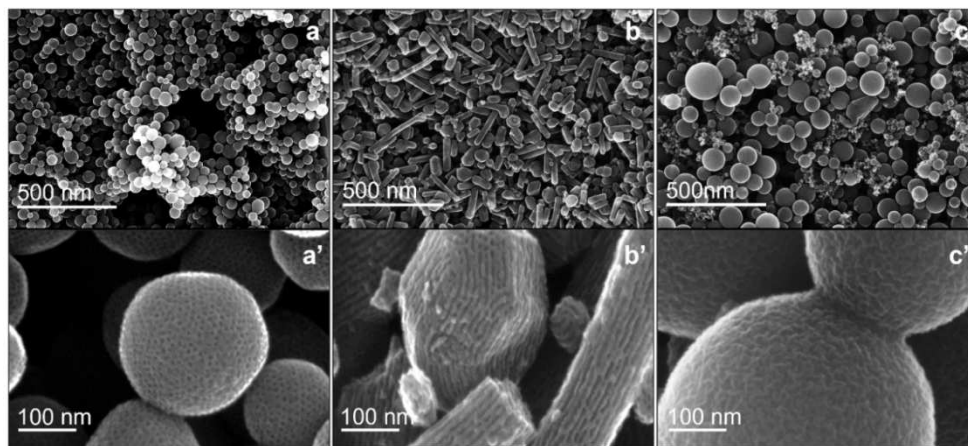


Figure 1. SEM images at different magnifications of PMT1:2 (a and a'), PMT1:3 (b and b'), and PM1:3 (c and c').

ization and the formation of conductive support. As discussed in the Supporting Information, thermogravimetric analysis (TGA) (Figure S2) allowed optimizing the experimental conditions for the thermal treatments of the samples (PMT1:2, PMT1:3, and PM1:3). The morphological characterization by SEM imaging enabled observing the nano-architecture of the synthesized materials. The PMT1:2 sample is characterized by uniform nanospheres with ~ 200 nm in diameter (Figure 1a) and a well-defined honeycomb porosity as evident from the highest magnitude SEM Figure 1a'. Differently, the PMT1:3 sample (Figure 1b and 1b') shows a non-homogeneous distribution of the particles in terms of shape and size. This is ascribable to the effect of the different precursor ratios, which gradually transformed the micelle structure from spherical to cylindrical.^[53] Also, PM1:3 (Figure 1c) shows spherical particles with very different sizes, which diameters range from 70 to 500 nm, indicating that during the polymerization step, the organic precursors (P and M) are not homogeneously distributed in the core structure led by Pluronic F127. Moreover, the resulting nanoparticles are rough-surfaced and not porous as the other samples (Figure 1c').

The porous structure and specific surface area (SSA) of each sample were derived from the adsorption isotherms (Figure 2a) using the Brunauer-Emmett-Teller (BET) model. The PMT1:2 sample showed the highest surface area of $1455 \text{ m}^2 \text{ g}^{-1}$, while PMT1:3 and PM1:3 had an SSA of $1124 \text{ m}^2 \text{ g}^{-1}$ and $994 \text{ m}^2 \text{ g}^{-1}$,

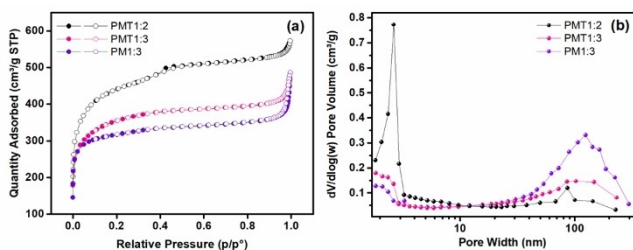


Figure 2. PMT1:2, PMT1:3 and PM1:3 (a) N_2 adsorption/desorption isotherms and (b) pore size distribution.

respectively.^[54,55] N_2 adsorption-desorption analysis (77.35 K), (Figure 2a and Figure S4a) reveals both types I and IV isotherms, the characteristic profile of disordered activated carbon.^[56] The typical hierarchical porous carbon profile can be predicted from hysteresis, which reveals the presence of meso and macroporosity and extended microporosity from the nonhorizontal plateau (at relative pressures $> 0.1 \text{ p/p}^0$).^[57-59] The observed slope is thus associated with mesopore filling. Moreover, the pore size distribution, estimated by the Barrett-Joyner-Halenda (BJH) method, also showed different results for the three samples (Figure 2b). The PMT1:2 possess pores predominantly in the range of 2 and 3 nm, with a maximum pore volume found at 2.6 nm. For the PMT1:3 and PM1:3 samples pore size mostly ranged between 2–3 and 50–260 nm. The electrocatalytic activity towards ORR of PMT1:2, PMT1:3, and PM1:3 was evaluated by linear sweep voltammetry (LSV) carried out using a three-electrode configuration in an O_2 -saturated alkaline environment (Figure 3). Overall, sample PMT1:2 showed the highest limiting current density ($J_{\text{lim}} = 3.74 \text{ mA cm}^{-2}$) as compared to PMT1:3 ($J_{\text{lim}} = 3.08 \text{ mA cm}^{-2}$), and PM1:3 ($J_{\text{lim}} = 2.52 \text{ mA cm}^{-2}$). This finding can be ascribed to a greater

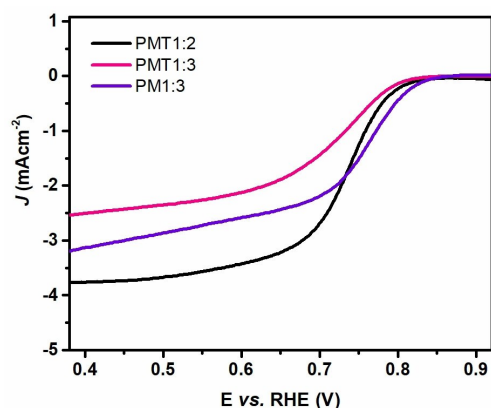


Figure 3. ORR polarization curves for PMT1:2, PMT1:3, and PM1:3 catalysts under O_2 -saturated KOH 0.1 M electrolyte at 1600 rpm and 5 mV s^{-1} scan rate.

homogeneity of particles in terms of shape and size, to a larger specific area, and to a high porosity that improves the exposure of C-N_x sites to the active species involved in the ORR.^[60,61] This confirms the critical role of morphology and porous distribution in the catalytic activity.^[62,63] Since PMT1:2 showed higher ORR activity as compared to PM1:3 and PMT1:3, it was chosen as C-N_x support for a subsequent functionalization with iron(II) to prepare the Fe–N–C mesoporous catalysts.

We prepared Fe–N–C catalysts by loading three different amounts of Fe onto the PMT1:2-based precursor (0.2, 0.5, and 1.3 wt.%). The actual iron load was also determined by inductively coupled plasma optical emission spectroscopy (ICP-OES). Iron was introduced by a further step in the above-described synthesis strategy (Scheme 1), adding a proper amount of iron (II) acetate to the precursor in ethanol solution. The samples are labeled as 0.2 Fe, 0.5 Fe, 1.3 Fe, and 0 Fe has been prepared for comparison. The transmission electron microscopy (TEM) images (Figures 4, S6 and S7) confirm that the material at the two concentrations has a porous structure with a regular texture (Figure 4a–d).

The energy dispersive X-ray analysis (EDX) (Figure 4e and f) indicated Fe dispersion over the carbon matrix characterized by

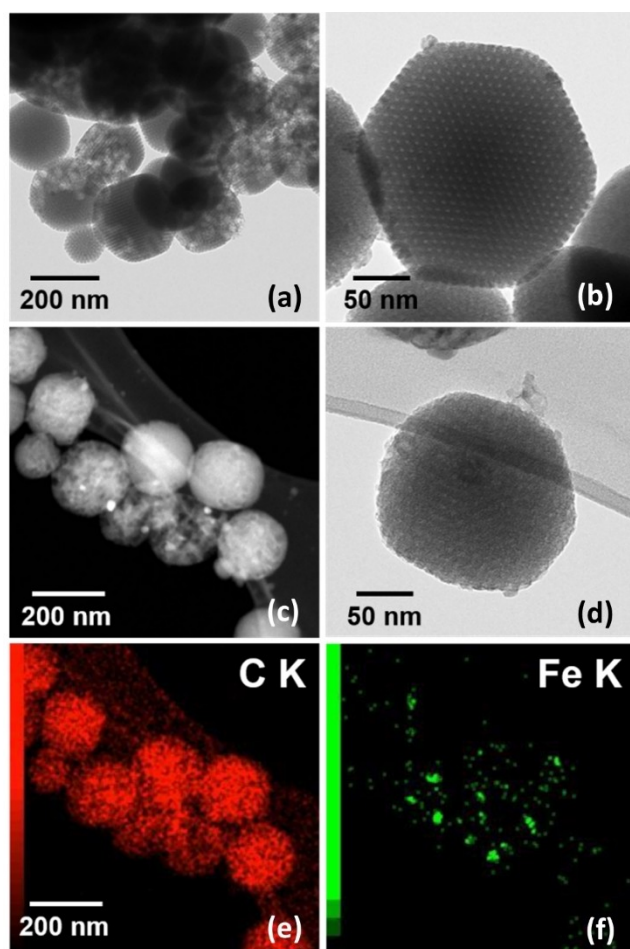


Figure 4. TEM images of a) 0.5 Fe and c) 1.3 Fe with b, d) corresponding close-up images of a single particle. EDX mapping images of 1.3 Fe with the corresponding e) C and f) Fe element.

different nm-sized particles. The more homogeneous distribution was found for the smaller nanoparticles, in comparison to the observed clusters (brightest spots in Figure 4f).

The N₂ isotherms profile for the Fe-functionalized materials (Figure S3a), indicated that SSA decreased with iron content increase (1022 ± 20 for 0.2 Fe, 704 ± 17 for 0.5 Fe and 512 ± 11 m² g⁻¹ for 1.3 Fe), while the pore size distribution, in terms of total micro, meso and macropore volume was similar (Figure S3). The total mesoporosity percentage for the metal-free carbon matrix (PMT1:2) was 58% and changed with Fe-functionalization to 65, 68 and 62% for 0.2 Fe, 0.5 Fe and 1.3 Fe, respectively. Similar to the pristine PMT1:2 material, the mesopores present in the 0.2 Fe, 0.5 Fe and 1.3 Fe catalysts were mostly found in a pore width range of 2 and 4 nm, as indicated by the pore size distribution (Figure S4a). In this range, the pore volume was more significantly affected by Fe-functionalization and decreased when the Fe load increased, corroborating the SSA trend.

The X-ray diffraction (XRD) patterns for the Fe–N–C catalysts are reported in Figure 5. The 0 Fe, 0.2 Fe, and 0.5 Fe samples showed the same broad peak in the intervals of $2\theta = 20^\circ - 30^\circ$ and $2\theta = 40^\circ - 50^\circ$, which is typical of carbonaceous amorphous materials after heat treatment and correspond to (002) and (101) plane of graphite phase, according to JCPDS reference pattern n° 00-003-0401.^[64,65] Secondary iron oxide phases (peak $2\theta = 35.6^\circ$) were found only for the sample with the highest Fe content. Moreover, for the 1.3 Fe catalyst, the (002) plane diffraction peaks at $2\theta = 26.0^\circ$ became more narrow and shifted positively, indicating the increase of graphitization degrees.^[66]

The surface chemistry of the iron-based and the undoped samples was evaluated by X-ray photoelectron spectroscopy (XPS) analysis. The full-width survey scan of the samples revealed the presence of four core levels, namely C 1s, N 1s, O 1s, and Fe 2p, among which C 1s and O 1s were predominant (Figure 6).

The C 1s spectra (Figure 7) for the Fe–N–C catalysts revealed the presence of multiple structures in a broad asymmetrical shape ranging from 284 eV to 293 eV. Starting from the lower binding energy (BE), it is possible to find: the defective

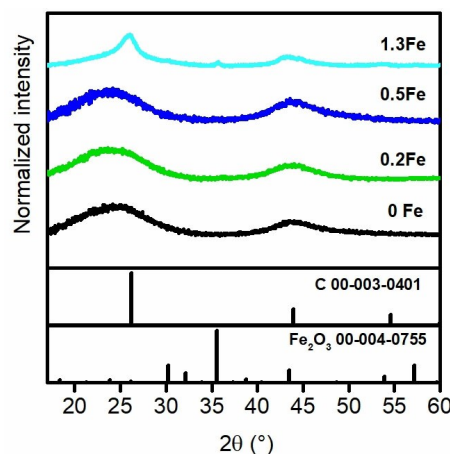


Figure 5. XRD patterns for the 0, 0.2, 0.5 and 1.3 Fe materials.

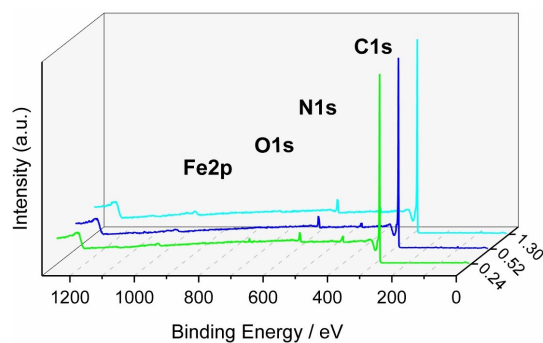


Figure 6. XPS survey scans for the 0.2, 0.5 and 1.3 Fe materials.

contribution (around 284 eV) ascribable to sp^3 C with pending bonds or amorphous phases, the graphitic sp^2 C (around 284.5 eV), the sp^3 C (C–C/C–H, ~285 eV), the C–N_x/C–OH (286–287 eV), various oxygenated species (287–290 eV).^[67–72] The 0.2 Fe and 0.5 Fe catalysts were characterized by a composite spectrum arising from the mixing of C 1s typical of polymers, centered at 285 eV and based on C–C sp^3 structures, and the C 1s of graphitic sp^2 domains, usually found at 284.5 eV. These two samples differ from the 1.3 Fe for the predominance of superposition of sp^3 and sp^2 contributions to the C 1s (Figure 7a and 7b). Indeed, 0.2 Fe and 0.5 Fe catalysts were characterized by a major sp^3 and/or amorphous phase structure, with the main peak centered at 284.8 eV. In this case, the structure can be ascribable to the low iron content, not capable of efficiently catalyzing the graphitization of the domains during pyrolysis.

Due to the low content of graphitic C for this category, the core level has been fitted using a standard Voigt function instead of the typical asymmetric Doniach-Sunjic function. 1.3 Fe had a main peak centered at 284.6 eV, more common to sp^2 carbon, and this predominant graphitic domain is in good agreement with XRD results (Figure 5). Upon comparison of the N 1s spectra (Figure 8), the differences found in the C 1s were lost, and the contributions to the deconvolution fits leveled. The chemical speciation of nitrogen has five contributions: pyridinic-N (398.5–398.8 eV), N coordinated to Fe (399.5–399.8 eV), protonated/pyrrolic N (400.6–400.9 eV), graphitic and quaternary N (401.5–402.5 eV), and oxides (above 403 eV).^[21,73] The spectra showed similar shape and width for all samples, characterized by two major components: pyridinic (N_{pyr}) and pyrrolic (N–H), followed by the nitrogen-coordinated Fe. Overall, the pyridinic form is found to be the main peak, except for Fe 1.3, where N_{pyr} and pyrrolic are comparable. Despite the differences in the iron content, the contribution of N_x-Fe is similar among the sample, with Fe 1.3 possessing a slightly higher amount.

The electrocatalytic ORR performance of 0.2 Fe, 0.5 Fe, and 1.3 Fe were evaluated by LSV with a rotating ring-disk electrode (RRDE). Figure 9 shows the ring currents and the disk current densities for all iron-based catalysts in comparison the undoped carbon supports. Table 1 lists all the electrochemical parameters extrapolated from the LSV-RRDE analysis. Even in a minimal percentage, the addition of iron significantly improves the ORR activity of the catalyst, positively shifting the potential from $E_{1/2} = 0.74$ V for 0 Fe to higher values around $E_{1/2} = 0.83$ V for the Fe–N–C sample.

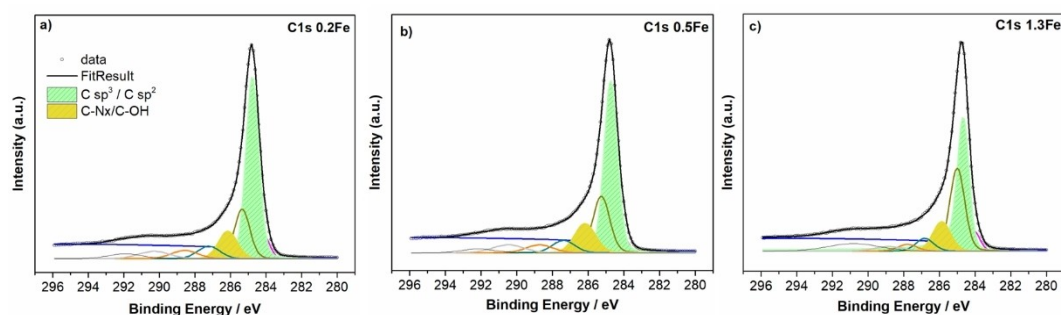


Figure 7. Deconvoluted high-resolution C 1s XPS spectra for: (a) 0.2 Fe; (b) 0.5 Fe, and (c) 1.3 Fe.

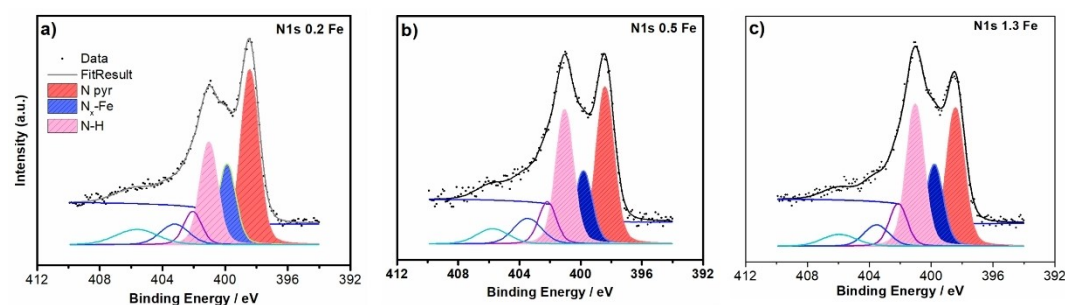


Figure 8. Deconvoluted high-resolution N 1s XPS spectra for: (a) 0.2 Fe; (b) 0.5 Fe and (c) 1.3 Fe.

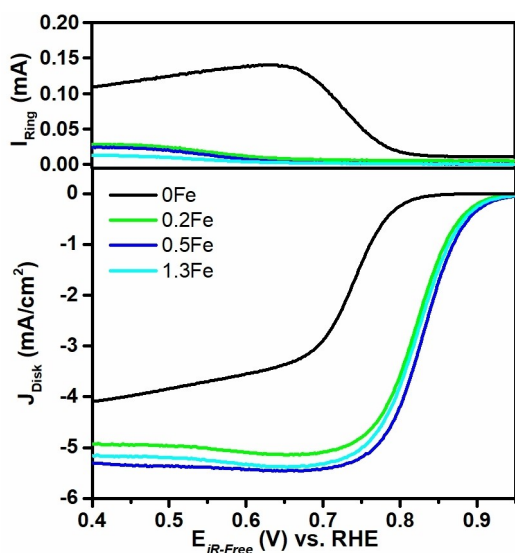


Figure 9. Ring currents (top panel) and disk current densities (bottom panel) under O_2 -saturated KOH 0.1 M electrolyte, at 1600 rpm and 5 mV s^{-1} scan rate for 0 Fe, 0.2 Fe, 0.5 Fe, and 1.3 Fe catalysts.

Table 1. ORR parameters for the Fe–N–C catalysts synthesized from different iron loads.

ORR parameters	0 Fe	0.2 Fe	0.5 Fe	1.3 Fe
E_{onset} [V]	0.80	0.92	0.93	0.92
$E_{1/2}$ [V]	0.74	0.82	0.84	0.83
J_{lim} at 0.4 V [mA cm^{-2}]	−4.0	−4.9	−5.4	−5.3
HO_2^- at 0.8 V [%]	95	4.2	1.2	0.9
n [0.8 V]	2.1	3.94	3.98	3.98
Tafel slope	55	–	58	60

As the iron content increases, the performances increase up to 0.5 wt.% iron content; after that, the performance reaches a plateau. In fact, the 0.5 Fe and 1.3 Fe samples showed similar performance with an $E_{1/2}$ of 0.84 V and 0.83 V, respectively, and a limiting current density calculated at 0.4 V J_{lim} of 5.4 and 5.3 mA cm^{-2} , respectively. Furthermore, in the mixed kinetic-diffusion-controlled region ($E = E_{1/2}$), the number of electrons exchanged (n), determined by Eq. 1 and Eq. 2, was 3.98 for both 0.5 Fe and 1.3 Fe, indicating that ORR mainly occurs through a direct $4e^-$ transfer mechanism.^[30,73] These parameters also confirm the high ORR activity of the prepared Fe–N–C materials as compared to the state-of-the-art Pt/C, which exhibits $E_{\text{onset}} = 0.96 \text{ V}$, $E_{1/2} = 0.91 \text{ V}$, and $J_{\text{lim}} = -5.5 \text{ mA cm}^{-2}$ (Figure S11b).

The ORR activity and mechanism at the surface of 0 Fe, 0.5 Fe, and 1.3 Fe electrodes were investigated from the Tafel plots, which were obtained by plotting iR -corrected potential values as a function of the logarithm of the kinetic current density, as shown in Figure S8. The plots were linearly fitted from the onset potential values (ca. 0.9 V for 0.5 Fe and 1.3 Fe, and 0.80 V for 0 Fe) to ca. 0.75 V vs. RHE, covering both the low current density (lcd) and the high current density (hcd) regions for the most active catalysts. From the linear region in the Tafel plot, which corresponds to a Tafel behavior, the exchange current density (J_0), was calculated after the determination of

the slope ($2.303RT/\alpha_c F$) and the intercept [$E^0 + (2.303RT/\alpha_c F) \log(J_0)$] respectively, according to Equation S1.^[74]

Tafel slopes around 60 mV dec^{-1} were observed for all samples over the investigated potential range, indicating that a similar mechanism governs ORR. According to the associative mechanism proposed by Shinagawa et al.^[75] the rate-determining step (rds) related to a 60 mV dec^{-1} Tafel slope in alkaline pH is characterized by a proton transfer from water to MO_2^- species, formed after the first electron transfer to adsorbed O_2 onto an empty active site (M): $\text{MO}_2^- + \text{H}_2\text{O} \rightleftharpoons \text{MO}_2\text{H} + \text{OH}^-$. Similar Tafel behavior has been also reported for other Fe–N–C materials with high ORR activity.^[76–80] Moreover, the activity trend observed from Tafel plots corroborates the LSV-RRDE analysis, with J_0 values two orders of magnitude higher for both 0.5 Fe and 1.3 Fe as compared to 0 Fe (Table S1), indicating the expected formation of more active catalytic sites with the Fe-functionalization.

In addition to the activity, ADTs were performed to assess the durability of the most active, Fe–N–C materials, since it is a key parameter for high-performance electrocatalysts. To evaluate the electrochemical surface area (ECSA) retention, a start-stop cycle durability test was performed for the 0.5 Fe and 1.3 Fe samples by acquiring cyclic voltammograms at 5 mV s^{-1} in the potential window between 0.6–1.2 V vs. RHE, after cycling the potential over 30000 cycles at a rate of 500 mV s^{-1} in N_2 -saturated electrolyte.^[81] The ECSA for 0.5 Fe and 1.3 Fe samples (Figure 10a and Figure S9a) was stable over cycling with only a 4% and 5% ECSA decrease, respectively. In terms of ECSA change during cyclic voltammetry (CV) cycles, the steady behavior of synthesized catalysts outperformed Pt/C taken as control that experienced a 65% ECSA loss after 30000 cycles (Figure 10b), in agreement with previous reports.^[81] Durability of the catalysts was also assessed by evaluating the ORR parameters changes ($E_{1/2}$ and J_{lim} @0.4 V vs. RHE) after 1 and 7500 CV cycling in N_2 -saturated 0.1 M KOH electrolyte (Figures S9b and S10), and compared with Pt/C (Figure S11).

Figure 10c reports $E_{1/2}$ changes after cycling for 0.5 Fe, 1.3 Fe, and Pt/C. After 1000 cycles, the 0.5 Fe and 1.3 Fe catalysts exhibited only a slight decrease in $E_{1/2}$ (less than 1.5%) while for Pt/C $E_{1/2}$ decrease of 17%. Moreover, after 7500 cycles, 0.5 Fe and 1.3 Fe show a decrease of 4.2% and 3.1%, respectively, indicating high performance durability the Fe–N–C catalysts compared to Pt/C. To get deeper insights on the catalyst's durability, a further ADT was also carried out by cycling the potential under O_2 -saturated electrolyte. The ORR parameters were extrapolated from the LSV curves after 1, 10 k, and 30 k CV cycles. Tests indicated that the presence of O_2 during the potential cycling significantly affects the ORR performance of the 0.5 Fe (Figures S9b and S12), as compared to the 1.3 Fe catalyst (Figure 10d and Figure S10). The $E_{1/2}$ decrease for 0.5 Fe was 4.9% after 10 k, and 7.3% after 30 k. For the more graphitic material, 1.3 Fe, $E_{1/2}$ decreased only 1.7% and 2.8% after 10 k and 30 k, respectively. 0.5 Fe and 1.3 Fe samples and Pt/C taken as control were assembled at the cathode side of a 5 cm^2 AEMFC fed with H_2 and O_2 and equipped with an FAA-3-50 membrane, to evaluate the performance under practical operation. Figure 11 shows the I - V

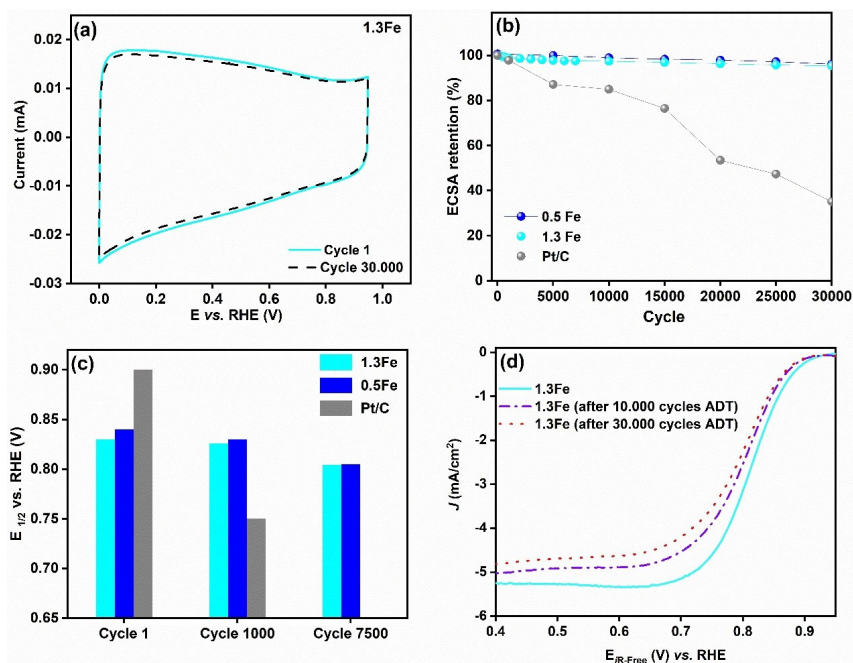


Figure 10. (a) CV of 1.3 Fe in N_2 -saturated electrolyte at scan rate of 5 mVs^{-1} before and after 30000 CV cycles. (b) ECSA retention over cycling. (c) $E_{1/2}$ changes for 0.5 Fe and 1.3 Fe and the Pt/C electrode taken as control. (d) LSV of 1.3 Fe before and after 10000 and 30000 potential cycles in O_2 -saturated electrolyte.

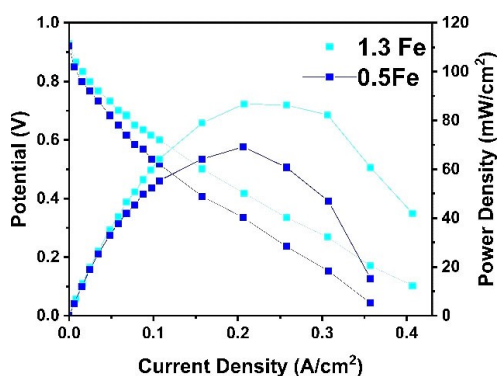


Figure 11. Polarization and power density curves for AEMFCs assembled with 0.5 Fe, 1.3 Fe (4.5 mg cm^{-2}) cathodes. 5 cm^2 AEMFC single cell with an FAA3-50 membrane at 60°C , 100% RH, 1 bar abs H_2/O_2 .

and power density curves obtained at 60°C and 100% of relative humidity (RH), and the corresponding electrochemical parameters are reported in Table 2.

The AEMFCs equipped with the Fe–N–C-based cathodes showed a promising performance in comparison to the state-of-

the-art Pt/C, in terms of open-circuit voltage (OCV), current and power density values. The maximum power density was higher for the sample with the highest iron content: an increment of about 20% in both current density (at 0.2 V) and power density is registered. This finding can be ascribed to the small but significant differences between 1.3 Fe and 0.5 Fe samples, as evidenced by physicochemical characterizations. Indeed, from a structural point of view, the 1.3 Fe catalyst has a more pronounced graphitic character, as pointed out by XRD and XPS analysis. Experimental analysis and density functional theory (DFT) calculations have demonstrated that graphitic carbon domains can enhance the intrinsic ORR activity of Fe–N_x–C active sites by optimizing their electronic structure, leading to a decrease in the adsorption energy for the ORR intermediates.^[78,82,83] Moreover, in comparison to amorphous carbon, graphitic domains in Pt-based and Fe–N–C catalysts were found to minimize the voltage loss induced by ohmic resistance and provide high chemical and electrochemical corrosion resistance to provide increased stability and durability for electrocatalysis.^[84,85] In fact, both 0.5 Fe and Fe 1.3 exhibited similar chemical surfaces in terms of high-active catalytic sites and ORR activity; however, performance durability in a half-cell configuration was higher for 1.3 Fe; despite its lower SSA ($512 \text{ vs. } 704 \text{ m}^2 \text{ g}^{-1}$) 1.3 Fe showed a higher contribution of graphitic carbon than 0.5 Fe.

This is in good agreement with the AEMFC tests in which 1.3 Fe outperformed the 0.5 Fe catalyst, indicating that highly graphitic domains played an essential role in the catalyst performance under operating conditions.

In Table 3, the performance of the H_2 -fed AEMFCs equipped with 0.5 Fe and 1.3 Fe at the cathode side and the FAA-3-50 membrane is compared to the performance of AEMFCs

Table 2. Electrochemical parameters for the tested MEAs assembled with the 0.5 Fe, 1.3 Fe and Pt/C (Pt loading 0.5 mg cm^{-2}) as cathode electrocatalysts of the H_2 -fed AEMFC.

Sample	OCV [V]	R_{cell} [$\Omega \text{ cm}^2$]	$E_{\text{cell}}@0.2 \text{ A cm}^{-2}$ [V]	Max PD [mW cm^{-2}]
0.5 Fe	0.92	0.325	0.335	69
1.3 Fe	0.93	0.315	0.418	87
Pt/C ^[97]	1.05	0.27	0.650	148

Table 3. AEMFC maximum power density values obtained with different PGM-free cathodes and AEMs.

Ref.	T_{cell} [°C]	Cathode catalyst loading [mg cm ⁻²]	Anode catalyst and Pt loading [mg cm ⁻²]	AEM	Max PD [mW cm ⁻²]
This work	60	0.5 Fe 4.5	Pt/C 0.50	FAA-3-50 FuMa-Tech	69
This work	60	1.3 Fe 4.5	Pt/C 0.50	FAA-3-50 FuMa-Tech	87
[86]	60	Fe-Fe ₂ O ₃ /NGr 3.0	Pt/C 0.35	FAA FuMa-Tech	54
[87]	50	NiCo-N-C 4.0	Pt/C 0.12	FAA-3-50 FuMa-Tech	65
[88]	50	FeN/CDC 1.5	Pt/C 0.46	Tokuyama A201	80
[89]	60	TiCDC/CNT (1:3)/FePc 2.0	PtRu/C 0.40	HMT-PMBI	182
[90]	60	FeS-iNC_50a 3.0	PtRu/C 0.24	FAA-3-50 Fuma-Tech	208
[91]	50	Fe-N-C 2.0	PtRu/C 0.40	HMT-PMBI	220
[92]	60	Fe-N-C-Gra 2.0	Pt/C 0.46	Tokuyama A201	243
[93]	65	CoFe-N-OMC/ CNT 1.0	PtRu/C 0.27	HMT-PMBI	336
[94]	50	FeN-SiCDC-0.5- 400-PVP 2.0	PtRu/C 0.53	HMT-PMBI	356

operating with different AEMs and similar PGM-free materials as a cathode catalyst. The maximum power density (Max PD) values indicate that catalysts' performance were comparable to or even higher than the obtained for other AEMFC tests in which similar Fuma-Tech membranes were used. These fuel cell test results can be considered very promising because they involve PGM-free catalysts embedded in a membrane-electrode structure not yet optimized. Better AEMFC performance could be achieved by optimizing the system in terms of electrode structure, and using different membranes and ionomers from FUMASEP® FAA-3-50.

Conclusion

We proposed a soft-template strategy as an efficient and innovative method to obtain nitrogen-doped carbon materials using organic precursors POP with different nano-architectures, obtained by changing the precursors' molar ratio: PMT1:2, PMT1:3, and PM1:3. Soft templating had an essential role in the construction of an extended porous structure because it coordinates phenol-melamine polymer with differently shaped shells, and it is blandly removed during pyrolytic treatment. PMT1:2 exhibited a well-developed hierarchical structure, and it has been doped with different iron contents (0.2–1.3 wt.%). Fe-N-C catalysts with a homogenous dispersion of Fe, and remarkable large surface area (512 to 1022 m²g⁻¹), depending on the iron content, and large pore volume has been prepared. The samples functionalized with 0.5%Fe and 1.3%Fe samples

showed excellent ORR activity in terms of half-wave potential (0.84 and 0.83 V vs. RHE, respectively), low HO₂⁻ yield (1.2% and 0.9%, respectively), the number of electrons transferred (close to 4e⁻), and high stability compared with the Pt/C benchmark in alkaline media (pH = 13). Tests conducted in a H₂-fed AEMFC indicated a good electrochemical performance for both 1.3 Fe and 0.5 Fe samples, pointing at POP-based Fe-N-C catalysts as promising candidates to assemble PGM-free H₂-fed AEMFCs.

Experimental Section

Essential materials

Melamine (M) (98.0%), phenol (99.5%), iron(II) acetate (95.0%), formaldehyde solution (37 wt.% in H₂O), Pluronic F127, Nafion solution (5 wt.% in lower aliphatic alcohols and water, 15–20%), and 2-propanol were purchased from Sigma-Aldrich. Platinum, nominally 40% on carbon black (Pt/C) was purchased by Alfa Aesar. Millipore water (Merk, 18.2 MΩ cm) was used for materials preparation and experiments.

Catalysts preparation

In this work, several samples were prepared and investigated: PMT1:2; PMT1:3; PM1:3 [different phenol (P) and melamine (M) molar ratio, with or without Pluronic F127 (T)] and 0 Fe; 0.2 Fe; 0.5 Fe and 1.3 Fe [precursors molar ratio is fixed (PMT1:2) and differ for the iron content]. For the materials synthesis, 0.796 g of phenol and 2.13 g melamine (2.38 for the sample PM1:3 and PMT1:3) are added to 15 mL of NaOH 0.1 M solution and kept under stirring at 50 °C until complete solubilization. Next, 2.2 mL of a formaldehyde solution (37 wt.% in H₂O) was added to the mixture and kept at 70 °C for 30 minutes. After that, when the mixture temperature reached 60 °C, 0.96 g of Pluronic F127 in 15 mL of water was added. In the case of PM1:3, 15 mL of pure water was added to maintain the same volume. After 2 hours, 50 mL of water was added, and the reaction mixture was kept under stirring at 60 °C overnight. After cooling to room temperature, 30 mL of the resulting solution was diluted with 112 mL of distilled water, transferred to a Teflon-coated autoclave, and heated to 120 °C for 24 hours. The obtained polymer was washed, filtered, and dried in an oven at 50 °C; the pyrolysis was carried out to get the PMT1:2, PMT1:3, PM1:3 samples. To prepare the Fe-N-C catalyst, the polymer matrix obtained after the hydrothermal phase was impregnated with proper amounts of Fe^{II}-acetate dispersed in 30 mL ethanol and left under stirring at room temperature overnight. The resulting composite material was dried at 50 °C and pyrolyzed with the procedure described below.

The pyrolysis process is the same for all samples, and it occurs at different ramp temperatures 5 °C min⁻¹ up to 250 °C, 1 °C min⁻¹ from 250 °C to 600 °C, 10 °C min⁻¹ from 600 °C to 900 °C. Carbonization took place under inert conditions (Ar) up to 900 °C. After this step, the sample remained at 900 °C in NH₃ flow for 20 minutes.

Materials characterization

Physicochemical characterization

TGA was performed by using a thermogravimetric analyser TGA/DSC1 Star System (Mettler Toledo) working under an N₂ flow

between 25 to 1000 °C, with a heating rate of 20 °C min⁻¹. The materials were held in a platinum sample holder with a cover having one central vent hole.

The samples stoichiometry was analyzed by ICP-OES (Varian 710-ES).

N₂-adsorption-desorption analysis was performed by Micromeritics® TriStar II Plus. BET method was used to calculate the specific surface area, and the pore volume was deduced by the adsorbed quantity of nitrogen at $p/p_0 = 0.99$. The pore size distribution was calculated by the BJH model of the desorption isotherm in the range of 2~250 nm. Samples were carefully prepared before measurements to remove possible impurities that might have adsorbed in the air; they were kept at 250 °C for 4 h under vacuum and then placed in sample holders for measurement of N₂ desorption.

Powder XRD patterns were recorded using Philips PW1730 diffractometer with Cu K α radiation ($\lambda = 1.5406$ Å). Micrographs were obtained using a SEM Leo Supra 35 field-emission scanning electron microscope (Carl Zeiss, Oberkochen, Germany).

TEM specimens were prepared by dispersing the powders in ethanol and drop-casting them onto holey carbon film on Cu grids. Bright-field TEM analyses were performed with a JEOL JEM-1011 TEM operated at 100 kV. EDX was obtained with a scanning transmission electron microscope (STEM, JEM-1400Plus) with analytical double-tilt holder operated at 120 kV.

The compositional analysis and chemical speciation of the samples were performed by exploiting the XPS technique in Ultra High Vacuum (UGV, < 10⁻⁹ mBar). The instrumentation used is a SPECS PHOIBOS 150 XPS system equipped with a monochromatic Al K α (1486.6 eV) X-ray source (XR50 MF) and high-speed imaging 2D CMOS true counting detector.

Electrochemical characterization

Electrochemical tests were performed using a standard three-electrode cell: a rotating ring disk electrode (RRDE-AFE6R2GCPT, Pine Research Instrumentation) and rotating disk electrode (RDE-AFE4R2GCPT Pine Research Instrumentation) were used as working electrode (WE), whereas a graphite rod and saturated silver chloride electrode (Ag/AgCl 3.3 M) as counter and reference electrodes, respectively. The measurements were recorded with a VMP3 Potentiostat (Bio-Logic Science Instruments) controlled by a computer through EC-Lab V10.18 software. The potential values for all electrochemical tests were measured vs. Ag/AgCl and converted to the reversible hydrogen electrode (RHE).

Prior to the deposition of the catalyst ink, surface of the WEs was mechanically cleaned in an Alumina slurry dispersion (0.05 μ m, Pine) by using a micro cloth pad. The WEs were further rinsed with deionized water (DI) and finally ultrasonicated at room temperature in DI for 5 minutes. The catalyst ink was prepared with 3.4 mg of catalyst were dispersed in 425 mL of 2-propanol and 75 μ L Nafion/H₂O solution (0.5 wt.%). The suspension was ultrasonicated for 2 h at room temperature. The ink was dropped onto the glassy carbon disk of the WE to a catalyst loading of 0.20 mg cm⁻², and dried in a ventilated stove at 40 °C for 1 min. A Pt/C ink was also prepared to a 16 μ g cm⁻² Pt loading and taken as control.

The electrodes were placed in a KOH 0.1 M electrolyte solution, saturated with N₂ for 20 min. Before acquiring electrochemical measurements, the WE (disk and ring) surface was electrochemically cleaned by using CV cycling in a potential window 1.2–0.3 V at a scan rate of 500 mV s⁻¹ (200 cycles). The ohmic resistance of the systems was also evaluated by *iR* determination and compensation by impedance spectroscopy.^[95]

After appropriately saturating the electrolyte with oxygen, LSV curves were acquired with RRDE. Experiments were performed at a scan rate of 5 mV s⁻¹ and rotation speed of 1600 rpm from 1.0 to 0.0 V, with the Pt ring polarized at 1.2 V. Disk and ring currents were background corrected by subtracting the capacitive current measured in N₂-saturated electrolyte, and the potentials reported were *iR*-compensated. The number of electrons transferred (*n*) and hydroperoxide anion (HO₂⁻) produced were calculated according to Eqs. (1) and (2), where *N* is the ring collection efficiency (0.26):

$$n = \frac{4 \times |I_{\text{Disk}}|}{|I_{\text{Disk}}| + |I_{\text{Ring}}/N|} \quad (1)$$

$$\text{HO}_2^- [\%] = 200 \times \frac{|I_{\text{Ring}}/N|}{|I_{\text{Disk}}| + |I_{\text{Ring}}/N|} \times 100 \% \quad (2)$$

ADTs were carried out to investigate the durability performance of the synthesized Fe–N–C catalysts. The experiments were performed by recording CV at a scan rate of 500 mV s⁻¹ in N₂-saturated electrolyte to evaluate the ECSA changes between 0.6–1.0 V vs. RHE over 30000 cycles. These potential cycling conditions were adopted to investigate the durability of the Fe–N–C catalysts as compared to the state-of-the-art Pt/C over 7500 cycles. A further ADT was carried out by cycling the potential under O₂-saturated electrolyte over 30000 CV cycles to better assess the Fe–N–C catalyst's durability.^[96]

AEMFC tests

Electrodes and MEAs preparation

The 0.5 Fe and 1.3 Fe samples were used for the cathode electrode preparation. The catalytic ink was obtained by mixing in an ultrasonic bath the electrocatalyst and FAA3 ionomer with an 80/20 wt.% ratio, as elsewhere reported.^[97] The ink was deposited by spray coating technique onto a Sigracet 25-BC gas diffusion layer (SGL). A catalyst loading of 4.5 mg cm⁻² was reached. As the anode, an electrode with a Pt loading of 0.5 mg cm⁻² was prepared by mixing the commercial 40 wt.% platinum on carbon (Pt/C) electrocatalyst (Alfa Aesar) and the FAA3 ionomer, by maintaining a ratio of 80/20 wt.%, by following a procedure reported elsewhere.^[98] A Fumasep® FAA3-50 membrane (FuMa-Tech), previously exchanged in hydroxylic form, was used as the electrolyte.^[99] A cold-press procedure was used to realize the membrane-electrode assemblies (MEAs).^[100]

Electrochemical characterization

The MEAs prepared as above reported were placed in a 5 cm² single cell. The cell hardware was connected to a commercial test station (Fuel Cell Tech.) equipped with an electronic load. The AEMFC performance in terms of polarisation and power density curves was evaluated in the following operative conditions: 60 °C, H₂/O₂ fully humidified with a flow rate of 1.5 and 2 times the stoichiometric value at each imposed current intensity. The electrochemical analyses were carried out using an AUTO LAB Potentiostat/Galvanostat (Metrohm), equipped with a 20 A current booster.

Acknowledgements

This work has received funding from: Regione Lazio through the project POR FESR LAZIO2014–2020, N^o A0375-2020-36492. A.C.

acknowledges the financial support i) the project “GEMIS – Graphene-enhanced Electro Magnetic Interference Shielding,” with the reference POCI-01-0247-FEDER-045939, co-funded by COM-PETE 2020 – Operational Programme for Competitiveness and Internationalization and FCT – Science and Technology Foundation, under the Portugal 2020 Partnership Agreement, through the European Regional Development Fund (ERDF). The authors acknowledge Luca Leoncino and Simone Lauciello (EM Facility of Istituto Italiano di Tecnologia) for TEM data acquisition and elaboration.” The integrated XPS were carried out at the SmartLab departmental laboratory of the Department of Physics at Sapienza University of Rome. EP and VCAF are grateful to Dr. M. Sbroscia for his assistance during the measurements.

Conflict of Interest

The authors declare no conflict of interest.

Data Availability Statement

The data that support the findings of this study are available from the corresponding author upon reasonable request.

Keywords: alkaline fuel cells · Fe–N_x–C active sites · mesoporous carbon · oxygen reduction reaction · platinum group metal-free electrocatalysts

- [1] I. Staffell, D. Scamman, A. Velazquez Abad, P. Balcombe, P. E. Dodds, P. Ekins, N. Shah, K. R. Ward, *Energy Environ. Sci.* **2019**, *12*, 463–491.
- [2] Z. Abidin, A. Zafaranloo, A. Rafiee, W. Mérida, W. Lipiński, K. R. Khalilpour, *Renewable Sustainable Energy Rev.* **2020**, *120*, 109620.
- [3] B. P. Sandaka, J. Kumar, *Chem. Eng. J. Adv.* **2023**, *14*, 100442.
- [4] A. Alzahrani, S. K. Ramu, G. Devarajan, I. Vairavasundaram, S. Vairavasundaram, *Energies* **2022**, *15*, 7979.
- [5] S. Choi, J. H. Drese, C. W. Jones, *ChemSusChem* **2009**, *2*, 796–854.
- [6] K. Jiao, J. Xuan, Q. Du, Z. Bao, B. Xie, B. Wang, Y. Zhao, L. Fan, H. Wang, Z. Hou, S. Huo, N. P. Brandon, Y. Yin, M. D. Guiver, *Nature* **2021**, *595*, 361–369.
- [7] Y. C. Lu, Z. Xu, H. A. Gasteiger, S. Chen, K. Hamad-Schifferli, Y. Shao-Horn, *J. Am. Chem. Soc.* **2010**, *132*, 12170–12171.
- [8] Y. Kang, X. Ye, J. Chen, Y. Cai, R. E. Diaz, R. R. Adzic, E. A. Stach, C. B. Murray, *J. Am. Chem. Soc.* **2013**, *135*, 42–45.
- [9] D. R. Dekel, *J. Power Sources* **2018**, *375*, 158–169.
- [10] Y. Kang, C. B. Murray, *J. Am. Chem. Soc.* **2010**, *132*, 7568–7569.
- [11] C. Wang, H. Daimon, T. Onodera, T. Koda, S. Sun, *Angew. Chem.* **2008**, *120*, 3644–3647; *Angew. Chem. Int. Ed.* **2008**, *47*, 3588–3591.
- [12] G. Wu, K. L. More, C. M. Johnston, P. Zelenay, *Science* **2011**, *332*, 443–447.
- [13] M. M. Hossen, K. Artyushkova, P. Atanassov, A. Serov, *J. Power Sources* **2018**, *375*, 214–221.
- [14] E. Antolini, E. R. Gonzalez, *J. Power Sources* **2010**, *195*, 3431–3450.
- [15] B. Baruah, P. Deb, *Mater Adv* **2021**, *2*, 5344–5364.
- [16] R. Janarthanan, A. Serov, S. K. Pilli, D. A. Gamarra, P. Atanassov, M. R. Hibbs, A. M. Herring, *Electrochim. Acta* **2015**, *175*, 202–208.
- [17] X. Tan, S. Prabhudev, A. Kohandehghan, D. Karpuzov, G. A. Botton, D. Mitlin, *ACS Catal.* **2015**, *5*, 1513–1524.
- [18] C. H. Choi, M. Kim, H. C. Kwon, S. J. Cho, S. Yun, H. T. Kim, K. J. J. Mayrhofer, H. Kim, M. Choi, *Nat. Commun.* **2016**, *7*, 10922.
- [19] X. L. Tian, Y. Y. Xu, W. Zhang, T. Wu, B. Y. Xia, X. Wang, *ACS Energy Lett.* **2017**, *2*, 2035–2043.
- [20] A. Sarapuu, E. Kibena-Pöldsepp, M. m. Borgheib, K. Tammeveski, *J. Mater. Chem. A* **2018**, *6*, 776–804.
- [21] I. Matanovic, K. Artyushkova, P. Atanassov, *Curr. Opin. Electrochem.* **2018**, *9*, 137–144.
- [22] M. Hossen, S. Hasan, R. Islam, K. Tammeveski, P. Atanassov, *Appl. Catal. B* **2023**, *325*, 121733.
- [23] M. Risch, K. A. Stoerzinger, B. Han, T. Z. Regier, D. Peak, S. Y. Sayed, C. Wei, Z. Xu, Y. Shao-Horn, *J. Phys. Chem. C* **2017**, *121*, 17682–17692.
- [24] G. Faubert, G. Lalande, R. Côté, D. Guay, J. P. Dodelet, L. T. Weng, P. Bertrand, G. Dénès, *Electrochim. Acta* **1996**, *41*, 1689–1701.
- [25] H. Schulenburg, S. Stankov, V. Schünemann, J. Radnik, I. Dorbandt, S. Fiechter, P. Bogdanoff, H. Tributsch, *J. Phys. Chem. B* **2003**, *107*, 9034–9041.
- [26] H. Zhang, H. T. Chung, D. A. Cullen, S. Wagner, U. I. Kramm, K. L. More, P. Zelenay, G. Wu, *Energy Environ. Sci.* **2019**, *12*, 2548–2558.
- [27] Y. Han, Y. G. Wang, W. Chen, R. Xu, L. Zheng, J. Zhang, J. Luo, R. A. Shen, Y. Zhu, W. C. Cheong, C. Chen, Q. Peng, D. Wang, Y. Li, *J. Am. Chem. Soc.* **2017**, *139*, 17269–17272.
- [28] D. Xia, X. Yang, L. Xie, Y. Wei, W. Jiang, M. Dou, X. Li, J. Li, L. Gan, F. Kang, *Adv. Funct. Mater.* **2019**, *29*, 1906174.
- [29] H. T. Chung, J. H. Won, P. Zelenay, *Nat. Commun.* **2013**, *4*, 1922.
- [30] W. J. Jiang, L. Gu, L. Li, Y. Zhang, X. Zhang, L. J. Zhang, J. Q. Wang, J. S. Hu, Z. Wei, L. J. Wan, *J. Am. Chem. Soc.* **2016**, *138*, 3570–3578.
- [31] J. Zhang, Y. Zhao, C. Chen, Y. C. Huang, C. L. Dong, C. J. Chen, R. S. Liu, C. Wang, K. Yan, Y. Li, G. Wang, *J. Am. Chem. Soc.* **2019**, *141*, 20118–20126.
- [32] E. Proietti, F. Jaouen, M. Lefèvre, N. Larouche, J. Tian, J. Herranz, J. P. Dodelet, *Nat. Commun.* **2011**, *2*, 416.
- [33] C. Alegre, D. Sebastián, M. E. Gálvez, E. Baquedano, R. Moliner, A. S. Aricò, V. Baglio, M. J. Lázaro, *Materials (Basel)*. **2017**, *10*, 11–13.
- [34] R. Othman, A. L. Dicks, Z. Zhu, *Int. J. Hydrogen Energy* **2012**, *37*, 357–372.
- [35] Z. Chen, D. Higgins, A. Yu, L. Zhang, J. Zhang, *Energy Environ. Sci.* **2011**, *4*, 3167–3192.
- [36] J. H. Zagal, F. Bedioui, *Electrochemistry of N₄ Macrocyclic Metal Complexes: Volume 1: Energy, (Second Edition)*, **2016**, Springer Cham.
- [37] S. Das, P. Heasman, T. Ben, S. Qiu, *Chem. Rev.* **2017**, *117*, 1515–1563.
- [38] T. Pepè Sciarria, M. A. C. de Oliveira, B. Mecheri, A. D’Epifanio, J. L. Goldfarb, F. Adani, *J. Power Sources* **2020**, *462*, 228183.
- [39] T. Zhao, A. Elzatahry, X. Li, D. Zhao, *Nat. Rev. Mater.* **2019**, *4*, 775–791.
- [40] H. Shen, E. Gracia-Espino, J. Ma, H. Tang, X. Mamat, T. Wagberg, G. Hu, S. Guo, *Nano Energy* **2017**, *35*, 9–16.
- [41] D. S. Yang, D. Bhattacharjya, S. Inamdar, J. Park, J. S. Yu, *J. Am. Chem. Soc.* **2012**, *134*, 16127–16130.
- [42] Q. Yue, M. Wang, J. Wei, Y. Deng, T. Liu, R. Che, B. Tu, D. Zhao, *Angew. Chem.* **2012**, *51*, 10368–10372.
- [43] Q. Yue, J. Sun, Y. Kang, Y. Deng, *Angew. Chem. Int. Ed.* **2020**, *59*, 15804–15817.
- [44] Y. Zhou, Y. Yu, D. Ma, A. C. Foucher, L. Xiong, J. Zhang, E. A. Stach, Q. Yue, Y. Kang, *ACS Catal.* **2021**, *11*, 74–81.
- [45] Y. Wan, Y. Shi, D. Zhao, *Chem. Commun.* **2007**, *9*, 897–926.
- [46] L. Qin, Y. Wu, E. Jiang, *Energy* **2022**, *242*, 123040.
- [47] D. A. Frail, A. Wolszczan, *Nature* **1992**, *359*, 710–713.
- [48] D. Zhao, J. Feng, Q. Huo, N. Melosh, G. H. Fredrickson, B. F. Chmelka, G. D. Stucky, *Science*. **1998**, *279*, 548–552.
- [49] F. Schüth, *Chem. Mater.* **2001**, *13*, 3184–3195.
- [50] B. Mecheri, R. Gokhale, C. Santoro, M. A. Costa De Oliveira, A. D’Epifanio, S. Licocchia, A. Serov, K. Artyushkova, P. Atanassov, *ACS Appl. Energy Mater.* **2018**, *1*, 5755–5765.
- [51] Y. Wan, D. Zhao, *Chem. Rev.* **2007**, *107*, 2821–2860.
- [52] M. J. Fornerod, A. Alvarez-Fernandez, E. Williams, M. W. A. Skoda, B. Prieto-Simon, N. H. Voelcker, M. Stefik, M.-O. Coppens, S. Guldin, *ACS Appl. Mater. Interfaces* **2022**, *14*, 56143–56155.
- [53] L. Peng, H. Peng, Y. Liu, X. Wang, C. Te Hung, Z. Zhao, G. Chen, W. Li, L. Mai, D. Zhao, *Sci. Adv.* **2021**, *7*, eabi7403.
- [54] V. Gómez-Serrano, C. M. González-García, M. L. González-Martín, *Powder Technol.* **2001**, *116*, 103–108.
- [55] R. Bardestani, G. S. Patience, S. Kaliaguine, *Can. J. Chem. Eng.* **2019**, *97*, 2781–2791.
- [56] K. S. W. Sing, D. H. Everett, R. A. W. Haul, L. Moscou, R. A. Pierotti, J. Rouquerol, T. Siemieniowska, *Pure Appl. Chem.* **1985**, *57*, 603.
- [57] D. H. Everett, *Pure Appl. Chem.* **1972**, *31*, 579–638.
- [58] B. D. Zdravkov, J. J. Čermák, M. Šefara, J. Janků, *Cent. Eur. J. Chem.* **2007**, *5*, 385–395.
- [59] S. Lowell, J. E. Shields, M. A. Thomas, M. Thommas *Characterization of Porous Solids, Kluwer Academic Publishers, Dordrecht, Boston, London, 2004.*

- [60] E. Yeager, *J. Mol. Catal.* **1986**, *38*, 5–25.
- [61] R. Ma, G. Lin, Y. Zhou, Q. Liu, T. Zhang, G. Shan, M. Yang, J. Wang, *npj Comput. Mater.* **2019**, *5*, 522–529.
- [62] C. Cao, W. C. Chen, S. Tian, J. X. Chen, Z. Y. Wang, X. H. Zheng, C. W. Ding, J. H. Li, J. J. Zhu, Z. L. Zhu, Q. X. Tong, C. S. Lee, *Mater. Chem. Front.* **2019**, *3*, 1071–1079.
- [63] W. Li, C. Han, K. Zhang, S. Chou, S. Dou, *J. Mater. Chem. A* **2021**, *9*, 6671–6693.
- [64] L. Jiao, G. Wan, R. Zhang, H. Zhou, S. H. Yu, H. L. Jiang, *Angew. Chem. Int. Ed.* **2018**, *57*, 8525–8529; *Angew. Chem.* **2018**, *130*, 8661–8665.
- [65] H. Yang, X. Chen, W. T. Chen, Q. Wang, N. C. Cuella, A. Nafady, A. M. Al-Enizi, G. I. N. Waterhouse, G. A. Goenaga, T. A. Zawodzinski, P. E. Kruger, J. E. Clements, J. Zhang, H. Tian, S. G. Telfer, S. Ma, *ACS Nano* **2019**, *13*, 8087–8098.
- [66] F. J. Maldonado-Hódar, C. Moreno-Castilla, J. Rivera-Utrilla, Y. Hanzawa, Y. Yamada, *Langmuir* **2000**, *16*, 4367–4373.
- [67] B. Mecheri, V. C. A. Ficca, M. A. Costa de Oliveira, A. D'Epifanio, E. Placidi, F. Arciprete, S. Licocchia, *Appl. Catal. B* **2018**, *237*, 699–707.
- [68] W. da S. Freitas, A. D'Epifanio, V. C. A. Ficca, E. Placidi, F. Arciprete, B. Mecheri, *Electrochim. Acta* **2021**, *391*, 138899.
- [69] Y. Chen, R. Gokhale, A. Serov, K. Artyushkova, P. Atanassov, *Nano Energy* **2017**, *38*, 201–209.
- [70] Y. He, H. Guo, S. Hwang, X. Yang, Z. He, J. Braaten, S. Karakalos, W. Shan, M. Wang, H. Zhou, Z. Feng, K. L. More, G. Wang, D. Su, D. A. Cullen, L. Fei, S. Litsster, G. Wu, *Adv. Mater.* **2020**, *32*, 2003577.
- [71] K. Artyushkova, S. Rojas-Carbonell, C. Santoro, E. Weiler, A. Serov, R. Awais, R. R. Gokhale, P. Atanassov, *ACS Appl. Energ. Mater.* **2019**, *2*, 5406–5418.
- [72] I. Matanovic, K. Artyushkova, M. B. Strand, M. J. Dzara, S. Pylypenko, P. Atanassov, *J. Phys. Chem. C* **2016**, *120*, 29225–29232.
- [73] P. Qiu, F. Liu, C. Xu, H. Chen, F. Jiang, Y. Li, Z. Guo, *J. Mater. Chem. A* **2019**, *7*, 13036–13042.
- [74] R. Guidelli, R. G. Compton, J. M. Felici, E. Gileadi, J. Lipkowski, W. Schmickler, S. Trasatti, *Pure Appl. Chem.* **2014**, *86*, 259–262.
- [75] T. Shinagawa, A. T. Garcia-Esparza, K. Takanabe, *Sci. Rep.* **2015**, *5*, 13801.
- [76] D. Liu, B. Wang, K. Srinivas, B. Yu, X. Chen, F. Ma, X. Wang, X. Zhang, D. Yang, Y. Chen, *J. Alloys Compd.* **2022**, *901*, 17.
- [77] L. Chai, L. Zhang, X. Wang, L. Xu, C. Han, T. T. Li, Y. Hu, J. Qian, S. Huang, *Carbon* **2019**, *146*, 248–256.
- [78] S. Pérez-Rodríguez, D. Sebastián, C. Alegre, T. Tsoncheva, N. Petrov, D. Paneva, M. J. Lázaro, *Electrochim. Acta* **2021**, *387*, 138490.
- [79] L. Cao, X. Shi, Y. Li, X. Wang, L. Zheng, H. P. Liang, *Carbon* **2022**, *199*, 387–394.
- [80] F. He, X. Chen, Y. Shen, Y. Li, A. Liu, S. Liu, T. Mori, Y. Zhang, *J. Mater. Chem. A* **2016**, *4*, 6630–6638.
- [81] A. Zadick, L. Dubau, N. Sergent, G. Berthomé, M. Chatenet, *ACS Catal.* **2015**, *5*, 4819–4824.
- [82] X. Tao, R. Lu, L. Ni, V. Gridin, S. H. Al-Hilfi, Z. Qiu, Y. Zhao, U. I. Kramm, Y. Zhou, K. Müllen, *Mater. Horiz.* **2022**, *9*, 417–424.
- [83] J. Han, H. Bao, J. Q. Wang, L. Zheng, S. Sun, Z. L. Wang, C. Sun, *Appl. Catal. B* **2021**, *280*, 119411.
- [84] A. Bharti, G. Cheruvally, *J. Power Sources* **2017**, *360*, 196–205.
- [85] G. Wu, A. Santandreu, W. Kellogg, S. Gupta, O. Ogoke, H. Zhang, H. L. Wang, L. Dai, *Nano Energy* **2016**, *29*, 83–110.
- [86] S. K. Vishal, M. Dhavale, S. K. Singh, A. Nadeema, S. S. Gaikwad, *Nanoscale* **2015**, *7*, 20117–20125.
- [87] S. Hanif, N. Iqbal, X. Shi, T. Noor, G. Ali, A. M. Kannan, *Renewable Energy* **2020**, *154*, 508–516.
- [88] S. Ratto, I. Kruusenberg, M. Käärik, M. Kook, L. Puust, R. Saar, J. Leis, K. Tammeveski, *J. Power Sources* **2018**, *375*, 233–243.
- [89] R. Praats, M. Käärik, A. Kikas, V. Kisand, J. Aruväli, P. Paiste, M. Merisalu, J. Leis, V. Sammelseg, J. H. Zagal, S. Holdcroft, N. Nakashima, K. Tammeveski, *Electrochim. Acta* **2020**, *334*, 135575.
- [90] H. S. Kim, C. H. Lee, J. H. Jang, M. S. Kang, H. Jin, K. S. Lee, S. U. Lee, S. J. Yoo, W. C. Yoo, *J. Mater. Chem. A* **2021**, *9*, 4297–4309.
- [91] J. Lilloja, M. Mooste, E. Kibena-Pöldsepp, A. Sarapuu, B. Zulevi, A. Kikas, H.-M. Piirsoo, A. Tamm, V. Kisand, S. Holdcroft, A. Serov, K. Tammeveski, *J. Power Sources Adv.* **2021**, *8*, 100052.
- [92] R. Sibul, E. Kibena-Pöldsepp, S. Ratto, M. Kook, M. T. Sougrati, M. Käärik, M. Merisalu, J. Aruväli, P. Paiste, A. Treshchalov, J. Leis, V. Kisand, V. Sammelseg, S. Holdcroft, F. Jaouen, K. Tammeveski, *ChemElectroChem* **2020**, *7*, 1739–1747.
- [93] J. Lilloja, M. Mooste, E. Kibena-Pöldsepp, A. Sarapuu, A. Kikas, V. Kisand, M. Käärik, J. Kozlova, A. Treshchalov, P. Paiste, J. Aruväli, J. Leis, A. Tamm, S. Holdcroft, K. Tammeveski, *Electrochim. Acta* **2023**, *439*, 141676.
- [94] S. Ratto, A. Zitolo, M. Käärik, M. Merisalu, A. Kikas, V. Kisand, M. Rähn, P. Paiste, J. Leis, V. Sammelseg, S. Holdcroft, F. Jaouen, K. Tammeveski, *Renewable Energy* **2021**, *167*, 800–810.
- [95] K. Shinozaki, J. W. Zack, R. M. Richards, B. S. Pivovar, S. S. Kocha, *J. Electrochem. Soc.* **2015**, *162*, F1144–F1158.
- [96] K. Kumar, L. Dubau, M. Mermoux, J. Li, A. Zitolo, J. Nelayah, F. Jaouen, F. Maillard, *Angew. Chem.* **2020**, *132*, 3261–3269; *Angew. Chem. Int. Ed.* **2020**, *59*, 3235–3243.
- [97] W. da Silva Freitas, B. Mecheri, C. Lo Vecchio, I. Gatto, V. Baglio, V. C. A. Ficca, A. Patra, E. Placidi, A. D'Epifanio, *J. Power Sources* **2022**, *550*, 232135.
- [98] A. Carbone, R. Pedicini, I. Gatto, A. Saccà, A. Patti, G. Bella, M. Cordaro, *Polymer* **2020**, *12*, 283.
- [99] C. Lo Vecchio, A. Carbone, S. Trocino, I. Gatto, A. Patti, V. Baglio, A. S. Aricò, *Polymer* **2020**, *12*, 2991.
- [100] I. Gatto, A. Capri, C. Lo Vecchio, S. Zignani, A. Patti, V. Baglio, *Int. J. Hydrogen Energy* **2022**, DOI 10.1016/J.IJHYDENE.2022.04.176.

Manuscript received: November 28, 2022

Revised manuscript received: February 10, 2023

Version of record online: March 3, 2023